ASME Journal of Computing and Information Science in Engineering
Online journal at:
https://asmedigitalcollection.asme.org/computingengineering

Teaming Finite Element Analysis and Deep Learning to Advance Inverse Design of Metamaterial With Adaptive Pressure Response in Footwear Design

Ziyang Zhang
School of Industrial Engineering and Management,
Oklahoma State University,
Stillwater, OK 74078
e-mail: jan.zhang@okstate.edu

Yu Feng[1]
School of Chemical Engineering,
Oklahoma State University,
Stillwater, OK 74078
e-mail: yu.feng@okstate.edu

Chenang Liu[1]
School of Industrial Engineering and Management,
Oklahoma State University,
Stillwater, OK 74078
e-mail: chenang.liu@okstate.edu

Metamaterials (MMs) offer a promising solution for footwear design by enabling spatially tunable mechanical responses associated with comfort-related considerations. However, the current application of MMs in footwear manufacturing remains relatively limited. Furthermore, effective optimization of MM structures under comfort-related mechanical considerations remains a largely unexplored space. This study explores a framework that teams finite element analysis (FEA) and deep learning (DL) to optimize MM-based shoe sole designs by using the individual plantar pressure distribution data. Specifically, the FEA is deployed to analyze the mechanical response of the sole, and it establishes links among pressure, deformation, and geometry, while a DL model is developed to map plantar pressure to MM lattice geometry. In our proposed method, a multimodal convolutional neural network (CNN) model is designed and trained to predict the optimized lattice-rod radii in MM based on multimodal input, including the pressure image, rod coordinates, and deformation data. The DL-optimized MM structures are subsequently validated through FEA simulations. With this proposed approach, this study conducted a case study relevant to potential footwear applications under a deformation-based surrogate objective. The results show that the proposed method achieves significant improvement in deformation–pressure alignment compared with a benchmark design. In summary, the proposed FEA–DL framework enables direct generation of optimized MM designs from user-specific plantar pressure and a surrogate design objective. This synergistic approach offers a promising pathway to achieve a customizable, efficient, high-performance, resource-conserving inverse design. [DOI: 10.1115/1.4071847]

Keywords: deep learning (DL), finite element analysis (FEA), footwear design, inverse design, metamaterial (MM), computer-aided design, data-driven engineering, engineering informatics, inverse methods for engineering applications, machine learning for engineering applications

1 Introduction

Metamaterial (MM) has been recognized for its benefits, such as absorbing energy, reducing impact forces, and potential in improving comfort [1–5]. Due to the complex structure of MM, obtaining the mechanical properties usually needs experiments, consuming a significant amount of time and resources. Such low efficiencies can be significantly improved using inverse design according to the recent literature [6]. In addition, the personalization of MM has not yet been widely explored in the footwear industry [7]. Therefore, the objective of this study is to enable efficient, customizable MM-based sole inverse design by developing a computational framework that teams finite element analysis (FEA) and a deep learning (DL) model.

1.1 Metamaterial and Its Applications.

In general, MM is a network-shaped porous structure, composed of lattices sized from 1 mm to 10 mm. MMs with different lattice structures differ in lightweight, strength, fracture resistance [8], vibration mitigation [9], energy absorbing [10], and vibration reduction [10]. MM's advantage in customization is that it can change the lattice structure to modify the mechanical characteristics according to the user-specific demand, which is difficult when using homogeneous materials, such as ethylene-vinyl acetate (EVA) or thermoplastic polyurethane [11,12]. Based on this advantage, MM could be applied to various engineering fields, such as healthcare, sports

[1]Corresponding authors.

Manuscript received September 19, 2025; final manuscript received April 21, 2026; published online May 20, 2026. Assoc. Editor: Krishnanand Kaipa.

equipment, and protective equipment [13], since it is capable of enhancing comfort in wearing [14], protecting against sports injuries [15], and alleviating pain from diabetic foot [9].

The MM mechanical characteristics are mainly determined by four aspects of its topology, i.e., constituent material, number of the smallest units (lattice) per unit space, lattice structure, and the dimension of each unit. Chen et al. [9] and Tobias et al. [16] investigated a set of lattice structures, including planar and three-dimensional, and provided a variety of excellent characteristics of MM for analysis and research. In the application of footwear, a recent study conducted by Amorim et al. [1] exemplifies how MMs can be customized to individual foot shapes by combining different lattice or Kirigami structures based on the unique user-specific plantar pressure maps. Hudak et al. [3] and Nickerson et al. [17] explored the impact of the lattice thickness and density on the mechanical properties in accommodative footwear. Most of the existing studies focus on modifying Voronoi wall thickness or altering the lattice types and densities, while the lattice topology (each rod's radius or shape) remains unexplored for user-specific adaptations [1,18–24].

While prior studies have demonstrated the feasibility of customizing footwear metamaterials through lattice type selection, density grading, or regional thickness variation, most existing approaches remain limited to coarse-grained or region-wise design parameters. In these methods, lattice properties are typically adjusted uniformly within predefined zones, and the internal topology of individual lattice members is not explicitly optimized [1,25–28].

Therefore, existing research lacks further investigation into the effect of lattice topology on the microscopic mechanical properties or the lattice dimensions on the macroscopic mechanical properties. To address such a knowledge gap, developing an efficient computational method for inverse design is a promising solution, which aims to achieve the capability of optimizing the structure of MM by individually adjusting each lattice rod, thereby altering the local and overall mechanical properties of the shoe sole under user-specific loading conditions.

1.2 Role of Comfort and Plantar Pressure in Footwear Design. It is believed that the footwear's flexibility, bending stiffness, lightweight, and conformity to the shape of the human foot are regarded as important factors influencing perceived wearing comfort [29]. However, using the same material for the sole implies identical mechanical properties [30]. To achieve better cushioning in heel and forefoot areas, adding specialized structures in different areas is a commonly applied approach, such as incorporating gas chamber designs in the forefoot and heel regions [31].

As the mechanical feedback of the sole in response to plantar pressure is widely considered to be closely related to comfort perception, support, and injury prevention, redistributing plantar pressure is a critical factor [32]. Alleviating high-pressure points and evenly redistributing plantar pressure has been shown to be associated with improved comfort-related outcomes [33]. To maximize comfort, footwear structures should be adapted to accommodate plantar pressure and foot geometry, providing cushioning and flexibility in areas of higher pressure while offering support in low-pressure areas [18,34].

However, most studies still rely on traditional materials and basic geometry. Meanwhile, few studies have conducted a quantitative analysis of the relationship between footwear design and comfort, since comfort is too subjective as a factor. Luckily, many studies have found that peak pressure and maximum resultant force on the sole significantly affect subjective comfort. Additionally, the hardness and the strain of the sole that undergoes under contact pressure, also play a crucial role in the user's wearing experience [35,36]. Goonetilleke [37] suggested using a touch sensation index to measure comfort in different areas of the foot, with the touch sensation index for each area assessed based on the pressure in that region. This perspective inspired this study to investigate whether the localized plantar sole strain patterns, which also align with the foot pressure distribution, could serve as a surrogate indicator of potential comfort enhancement. It is emphasized that such alignment does not directly quantify subjective comfort but rather provides a physics-informed proxy motivated by prior biomechanical findings. Following this direction, this study proposes to leverage the target deformation $T(x, y, z)$ and use it as input for a trained predictive model to generate an optimized MM structure. Besides, the mean squared error (MSE) can be used to evaluate if the resulting optimized MM designs from the predictive model can provide better deformation alignment than the under-optimized designs using the conventional approach. Therefore, to realize this goal, an effective and efficient computational approach for structure optimization is necessary to enhance the alignment between plantar pressure and localized strain under a surrogate formulation. With such a computational approach, if an expected target deformation is given, subjective comfort may be indirectly explored through its relationship with user-specific plantar pressure and the mechanical response of the sole, which is critical to the customization of the MM sole.

1.3 The Applications of Deep Learning Models in Inverse Design. According to the existing literature, the optimization of MM footwear remains insufficiently explored under comfort-related mechanical considerations, while studies on lattice or structural designs typically follow a posteriori workflow [9,38]. Specifically, this flow adopts a forward design approach, where structures are first designed and then tested to evaluate the performance of different designs to identify the optimal one [28,39]. While forward design can identify applicable designs, it falls short of achieving personalized customization, as a single structure usually cannot be optimal for everyone. To achieve such a goal, targeted inverse design could play a critical role, where optimized designs are directly generated based on specific needs.

The inverse design requires establishing the relationship between the input (e.g., user-specific biological features, such as plantar pressure, and mechanical design), the intermediate link (e.g., the mechanical response), and the goal (e.g., target mechanical response driven by user biomechanical input and user feedback). This can help to ensure that the design process is tailored to individual requirements, bridging the gap between biomechanics, material properties, and mechanical design objectives. Following this, with the assistance of the emerging DL models to quantify such a relationship, the resulting inverse-design model can thereby generate an optimized structure based on user-specific pressure distribution and the target mechanical response [27,40]. Recently, the involvement of DL models has already shown its feasibility and potential in advancing inverse design [41,42]. For example, Ha et al. [43] explored the application of DL in predicting the mechanical behavior of different MM lattices and realized the creation of MM based on nearly all possible uniaxial compressive stress–strain curves. Zheng et al. [44] realized the inverse generation of MM given the target mechanical properties with different DL models.

However, the above-mentioned and many existing inverse-design studies using DL mainly focus on homogenous lattice structure generation to achieve target mechanical properties [45,46]. Therefore, it remains understudied on how to identify inhomogeneous lattice structures by fully leveraging the high customizability potential of MM. Furthermore, most of the DL models adopted in the existing research mainly rely on single-modal or single-type inputs, where the lattice structure or MM structure is determined by target mechanical properties or deformation only. Consequently, the user-specific biological features and desired mechanical response rarely appear in the input at the same time, making it still challenging to better achieve customized inverse design. Meanwhile, such multimodality nature of the inputs also leads to the critical need for a tailored multimodal DL model and an efficient solution to ensure data availability.

1.4 Teaming Finite Element Analysis and Multimodal Deep Learning to Advance Inverse Design. To address the gaps mentioned above, it is critical to develop a new computational methodology for effective and efficient inverse design, which is expected to consider and leverage the high-resolution spatial distributions of deformation or pressure on soles. However, in engineering practice, experimentally testing the mechanical performance of MM soles can be time-consuming and costly. Besides, embedding sensors within a complex sole structure for actual measurements is also challenging. To overcome this bottleneck, the FEA modeling and simulation could be a promising solution to obtain high-resolution deformation and pressure distributions in an efficient and cost-effective manner [25–28].

First-principle-based FEA is a noninvasive, time-effective, and cost-saving computational method, eliminating the need for physical sensors that are difficult to integrate into complex structures and avoiding destructive testing [47]. Therefore, using FEA to obtain high-resolution spatial distribution variables of interest, such as deformation, stress, and strain, is achievable and can address the experimental deficiencies mentioned above [48]. With FEA, a 3D computer-aided design (CAD) model of the sole can be directly imported, and pressure can be applied at relevant locations to simulate the mechanical response of the sole. Afterward, the results can then be exported for further analysis [49,50].

Although FEA can analyze mechanical response given complex structures and user-specific pressure distributions, it still cannot directly generate an optimized MM sole structure. On the other hand, since the available high-resolution spatial data can greatly strengthen the DL model for inverse design, this study proposes to team DL and FEA to further facilitate the inverse design of the MM shoe sole.

Specifically, to make the MM structure more editable for desired characteristics, rod radii besides lattice types and density within a single lattice can differ, allowing for better alignment with the natural pressure distribution of the foot [1,51]. Thus, the DL model in this study focuses on generating MM shoe soles in an inverse manner to optimize lattice-rod radii based on users' plantar pressure and target characteristics. The DL model takes multimodal inputs, i.e., the user-specific plantar pressure image, predesigned sole structure information, and mechanical response data. As for the mechanical response data, the training data can be obtained from FEA simulations. In practice, the predesigned user-specific target deformation data $T(x, y, z)$, which represents a prescribed mechanical objective rather than a direct measure of comfort, will be utilized to generate the DL-optimized MM sole structure.

With this teaming mechanism, FEA and DL will serve as two major computational components to complement each other in the proposed inverse-design method, termed FEA–DL. In the proposed FEA–DL, the FEA simulates the mechanical response based on plantar pressure and structural information, providing training data for the DL model, which can handle multimodal input. Once trained, the multimodal DL model can take plantar pressure, structure information, and target deformation metric as inputs to predict the optimal MM shoe sole structure with improved agreement to the prescribed target deformation. Unlike prior inverse-design approaches that rely on single-modal inputs or homogeneous lattice assumptions [25–28], the proposed multimodal formulation explicitly fuses pressure, geometry, and deformation information, enabling localized rod-level optimization rather than global or region-averaged parameter tuning.

The major contribution of this study can be summarized by two main aspects: (1) this study develops a systematic workflow mapping the plantar pressure to the MM shoe sole design and further validates the design with FEA and (2) with FEA, this study further explores how to adopt DL models to map the objective features from FEA results and plantar pressure to shoe sole geometry, which realizes shoe sole inverse design and customization. The rest of this article is organized as follows. Section 2 discusses the details of the proposed approach. In Sec. 3, the case study and experimental results are provided to validate the effectiveness of the proposed design. Conclusions and future work are discussed in Sec. 4.

2 Methodology

This section presents the proposed computational methodology to team FEA and DL, namely, FEA–DL, to advance the inverse design of MM-based footwear. It includes an established FEA model for data generation (Sec. 2.1), a tailored DL model for inverse design modeling (Sec. 2.2), as well as a mechanism of FEA-based forward validation and design optimization (Sec. 2.3).

Figure 1 shows the framework of this research, while the FEA simulation model is shown in Step D of Fig. 1, and the DL model is shown in Step E of Fig. 1. Although this section focuses on methodology, utilizing the data and 3D models from Steps A to C of Fig. 1 is still necessary for better illustration. Data and 3D models used in this section include preprocessed plantar pressure, both in grayscale image and matrix format, MM shoe sole CAD model generated by RHINOCEROS 3D 7 (Robert McNeel & Associates TLM Inc., Seattle, WA) [52] based on X lattice structure, MM rod information in matrix format, and geometry information indicating the position of the MM rod and overall size. Details for experiments are presented in Sec. 3.

2.1 Finite Element Analysis for Data Generation. In the forward design of MM shoe soles, plantar pressure and MM structure are independent variables, while FEA results are dependent variables. However, the FEA model is crucial for MM's sole inverse design because FEA results are used as input into the DL model to predict the MM structure, connecting design parameters to target performance. The FEA in this study involves four main steps, i.e., importing 3D sole geometry, meshing, importing pressure data and boundary conditions, and FEA simulation (see Figs. 2(*a*)–2(*d*)). The FEA simulations were conducted using ANSYS MECHANICAL 2024R2 (Ansys Inc., Canonsburg, PA). The MM shoe sole 3D CAD model is generated in RHINOCEROS 3D 7, driven by the Grasshopper plugin IntraLattice [53]. The generated model can be imported into ANSYS MECHANICAL, as shown in Fig. 2(*a*).

The high-resolution plantar pressure map generated in Step A undergoes coordinate transformation and normalization to create a tabular file, which is then imported into ANSYS WORKBENCH. The processes of coordinate transformation and normalization are shown in Eq. (1), where $P_{\text{norm}}(x',y')$ represents the assumed plantar pressure at the transformed coordinates and $S(x, y)$ is the smoothed and normalized plantar pressure at position (x, y). $S_{\min} = \min_{x,y} S(x, y)$ is the minimum normalized grayscale value, and $S_{\max} = \max_{x,y} S(x, y)$ is the maximum normalized grayscale value. The scaling factors, i.e., 100/240 and 250/420, transform the original pixelwise coordinate to a millimeter coordinate. Besides, multiplying 400-kPa scales the normalized grayscale value to a pressure range of 0–400 kPa, as it is a commonly used range for plantar pressure [54]:

$$P_{\text{norm}}\left(x \cdot \frac{100}{240}, y \cdot \frac{250}{420}\right) = \frac{S(x, y) - S_{\min}}{S_{\max} - S_{\min}} \cdot 400 \text{ kPa} \tag{1}$$

In Fig. 2(*c*), a fixed support is applied to the bottom surface of the sole, while the plantar pressure is projected onto the upper surface normally downward. With applied pressure and fixed support, the simulation can then be conducted to collect the mechanical response of the structure, including results such as *Z*-direction deformation, equivalent stress, normal stress, equivalent elastic strain, stress intensity, and strain energy. Given the assumption of this study that local deformation–pressure alignment can serve as a physics-informed surrogate motivated by comfort-related considerations, *Z*-direction deformation is selected from the various simulation results as the target outcome to be

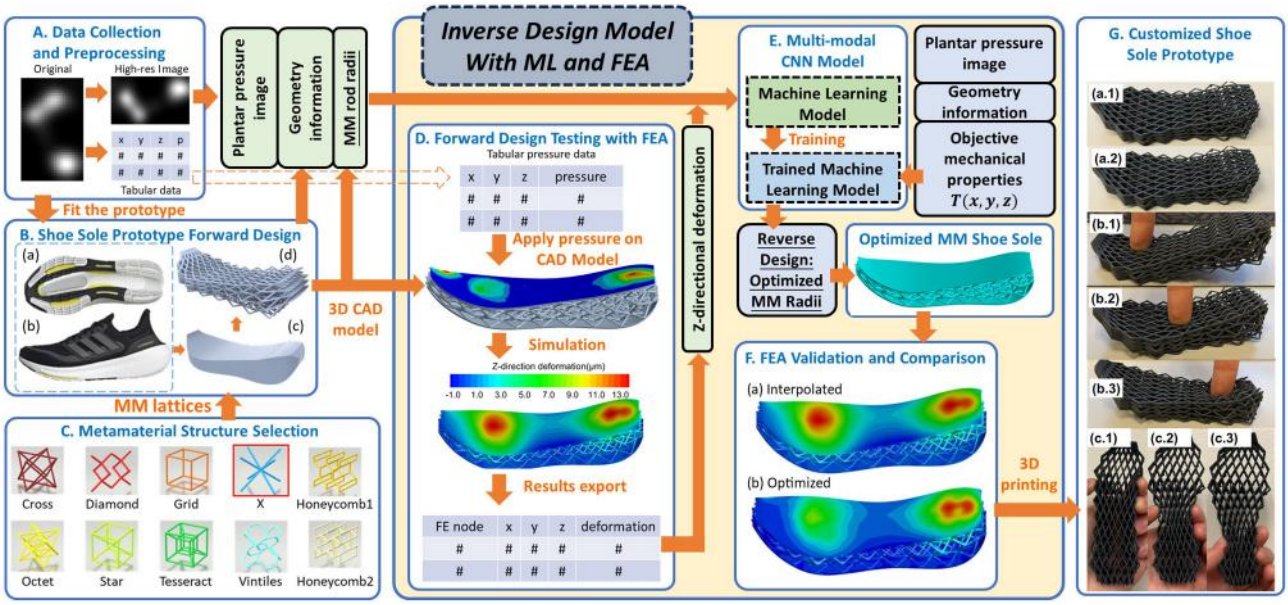

Fig. 1 Methodology workflow of the proposed inverse-design model integrating DL and FEA

collected in this step. Figure 2(*d*) shows the distribution of *Z*-direction deformation on the MM shoe sole geometry under applied plantar pressure, generated by simple optimization (i.e., linear interpolation). With the FEA model, simulation results, containing nodal coordinates and corresponding *Z*-direction deformations, will be exported as input for the DL model.

2.2 Multimodal Deep Learning-Based Inverse-Design Model. The tailored multimodal DL model in this study transforms traditional cyclic manufacturing-testing approaches by establishing quantitative mappings from user-specific data, structure information, and the target performance to the geometric design parameters. By correlating heterogeneous inputs with design parameters, the tailored DL model can overcome the designing-testing loop and thereby provide user-specific, real-time inverse design.

In this study, a multimodal convolutional neural network (CNN) model is designed and tailored to predict the rod radii of the MM shoe sole based on three types of input, namely, pressure distribution image, target stress-deformation data, and rod coordinates. This inverse-design model facilitates the customization of the MM shoe sole structure to better adapt to plantar pressure under a surrogate objective.

The tailored CNN model consists of three submodels, as shown in Fig. 3, including: (1) pressure image network: a 2D CNN processes pressure image data, which is resized and normalized to a fixed shape (240 × 420 pixels). This network extracts key spatial features of the plantar pressure distribution; (2) stress-deformation network: a 1D CNN handles the target stress-deformation data. These data are interpolated to a consistent shape and normalized. It represents the mechanical response under pressure conditions; and (3) rod coordinates network: another 1D CNN processes the rod coordinates of the MM structure. The model maintains the spatial arrangement of each rod by preserving its 3D coordinates (*X*,*Y*,*Z*) without flattening. The outputs of the three subnetworks are concatenated and passed through a series of fully connected layers. The final output layer predicts the radius for each rod in the MM structure, which is a list with a length of 640. In Fig. 1, the data used for training the DL model are backgrounded with light green, while the output of the DL model is underlined.

By training this model, this study aims to map the desired rod radii of the MM shoe sole given the user's plantar pressure, the coordinates of the rod midpoints in the MM CAD model, and the *Z*-direction deformation response. Thus, when applying the trained model, the required inputs include the user's plantar pressure data, the coordinates of the rod midpoints in the MM CAD model, and the target deformation for each element. The model then outputs the optimized radii for the MM shoe sole rods. When using the trained multimodal CNN model, the target deformation values are defined based on user-specific needs and are not derived from FEA simulation results. This approach allows customization of the shoe sole's mechanical properties to enhance deformation alignment according to individual preferences

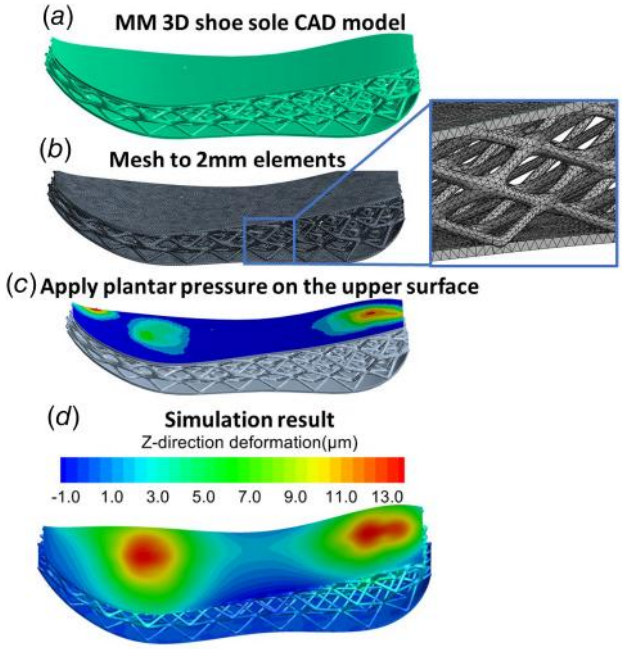

Fig. 2 FEA simulation details using the MM shoe sole: (*a*) CAD model import, (*b*) meshing, (c) fix support on the bottom surface and plantar pressure on top surface, and (*d*) *Z*-direction deformation

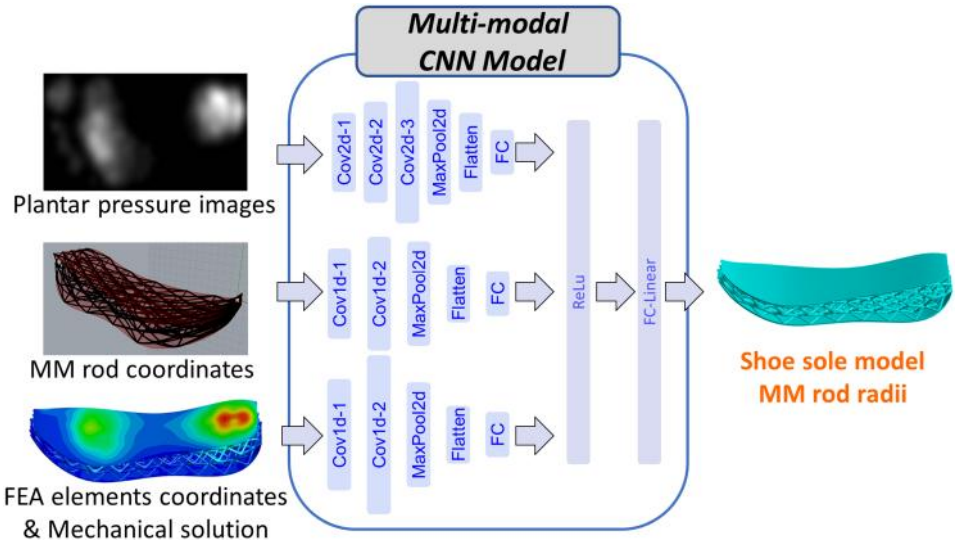

Fig. 3 An illustration of the tailored multimodal CNN model for inverse design

through optimization over each rod's dimension, aligning them with the user's unique plantar pressure profile.

2.3 Design Optimization and Finite Element Analysis-Based Forward Validation. Once the DL model is trained, the model will be used to generate the inverse-designed MM sole structure. FEA will be further used to validate the proposed design by comparing whether the proposed design has a better match to the plantar pressure than a benchmark.

To generate a DL-optimized MM shoe sole structure, it is essential to design the target deformation data. These data are generated by deriving the range of *Z*-direction deformation from the original FEA results and creating a pressure weight based on plantar pressure, along with a height weight based on the *Z*-coordinate. Equation (2) provides the mathematical expression for target deformation $T(x, y, z)$. Here, w_p is designed to induce greater deformation in areas with higher pressure, while w_z aims for larger deformations closer to the top surface. R_d refers to the range of *Z*-direction deformation. The formula $w_p(x, y) = p(x, y)/\text{Range}(P)$ refers to the plantar pressure weight, where $p(x, y)$ is the plantar pressure on interpolated coordinates (x, y). Furthermore, $w_Z(z) = (z - \min(Z))/\text{Range}(Z)$, which increases monotonically along the vertical direction and assigns a larger target deformation to points closer to the top surface. With the three inputs, the DL model can then generate optimized lattice radii, as shown in Fig. 1 (Step E):

$$T(x, y, z) = R_d \cdot w_p(x, y) \cdot w_z(z) \tag{2}$$

The MM shoe sole geometry generated based on the new plantar pressure image and target deformation will be simulated in ANSYS and compared with the MM shoe sole geometry created solely from plantar pressure by Step B of Fig. 1. To determine which of the two structures exhibits deformation that is more closely aligned with the plantar pressure distribution, a metric needs to be designed for comparison.

The metric used to evaluate the alignment between the target deformation and the actual deformation obtained from FEA is the MSE, as shown in the following equation:

$$\text{MSE} = \sum_{x,y,z} \frac{(T(x, y, z) - A(x, y, z))^2}{n} \tag{3}$$

Specifically, MSE is calculated by taking the square of the difference between the target deformation $T(x, y, z)$ and FEA-validated deformation $A(x, y, z)$ for each node from elements, summing these squared differences across all nodes, and then dividing by the total number of nodes n. The target deformation $T(x, y, z)$ is designed as a surrogate mechanical response that reflects desired alignment with plantar pressure distribution. The evaluation metric is therefore used to evaluate how well the FEA-validated deformation matches the prescribed target deformation, rather than serving as a direct measure of perceived comfort.

3 Case Study

The case study demonstrates a pipeline that personalizes an MM shoe sole from plantar pressure to a manufacturable design. Starting from a plantar pressure dataset, the dynamic pressure sequences are converted into static, high-resolution pressure images. The processed images are projected onto the sole to generate a linear-interpolated MM sole design and drive high-fidelity FEA over nine materials. With the linear-interpolated MM sole designs and FEA deformation data, a multimodal CNN model is trained. Performance is quantified through the MSE between the FEA-validated deformation and the prescribed target deformation $T(x, y, z)$, as well as the percentage reduction relative to the linear-interpolated baseline. Notably, as the linear interpolation method does not sufficiently optimize the structure according to the experiment results, the sole models generated through this method are referred to as "under-optimized" models.

3.1 Data Description and Preprocessing. The plantar pressure data is from the CAD WALK Healthy Controls Dataset [55], which contains the raw dynamic plantar pressure collected from 55 healthy Dutch individuals. For each individual, 24 trials were conducted to collect dynamic plantar pressure measurements from both feet. Each data sample contains 300–400 frames of dynamic pressure data, with each frame being an image approximately 40 pixels in length and 24 pixels in width. Since these data are nonstatic, low-resolution, and inconsistent in resolution, it needs to be converted into a static form, resized, and enhanced through denoising and smoothing to improve resolution for subsequent use. Figure 4 shows the framework of the preprocessing procedure.

Equation (4) shows that the static plantar pressure S_{pp} is obtained by taking the maximum value of the dynamic plantar pressure D_{pp} over the time series (frames). Equation (5*a*) shows the resizing process from static plantar pressure images to the target resolution image I using cubic interpolation. Equations (5*b*) and (5*c*) represent the scaling factors s_x and s_y, which determine the resizing ratios

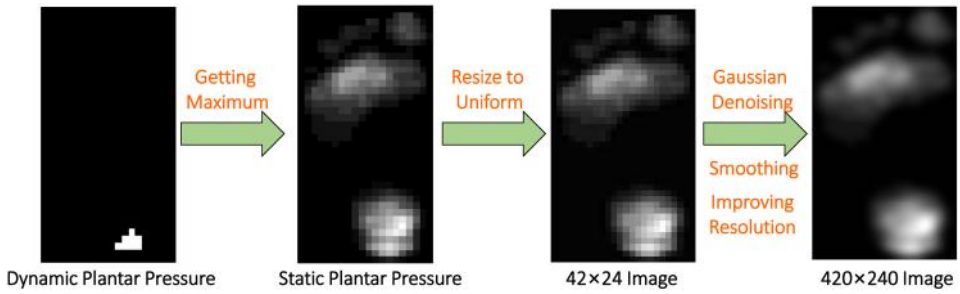

Fig. 4 The procedures of the plantar pressure data preprocessing

along the vertical and horizontal dimensions, where (T_x, T_y) denotes the target resolution and (S_x, S_y) denotes the original resolution:

$$S_{\mathrm{pp}(x,y)} = \max_t D_{\mathrm{pp}}(x, y, t) \tag{4}$$

$$I(x, y) = S_{\mathrm{pp}}(x \cdot s_x, y \cdot s_y) \tag{5a}$$

$$s_x = \frac{T_x}{S_x} \tag{5b}$$

$$s_y = \frac{T_y}{S_y} \tag{5c}$$

After this step, the images are resized to 42×24 pixels. Equation (6) demonstrates increasing the resolution of I to H by a factor z of 10 using cubic interpolation. This step improves the image's resolution to 420×240. Equation (7) demonstrates the use of Gaussian filtering on the H to further reduce noise, resulting in a smoother plantar pressure distribution S. u and v represent the relative displacement of neighboring pixels in the image. $\sigma = 6$ is the standard deviation of the Gaussian filter. For FEA, the pressure images are normalized to a range of 0–400 kPa as clarified and sampled to a XY-coordinate-based table [54]:

$$H(x, y) = I\left(\frac{x}{z}, \frac{y}{z}\right) \tag{6}$$

$$S(x, y) = \frac{1}{2\pi\sigma^2}\int_{-\infty}^{\infty}\int_{-\infty}^{\infty} H(x-u, y-v)\mathrm{e}^{\left(\frac{-u^2+v^2}{2\sigma^2}\right)} dudv \tag{7}$$

The processed high-resolution plantar pressure distribution map will: (1) be employed to generate the under-optimized MM shoe sole models, (2) serve as input for FEA to conduct mechanical analysis on the CAD model after normalization, and (3) be used as input for training the DL model and validating the inverse design.

3.2 Sole Outline. In this subsection, the sole geometry is first defined by constructing the upper and lower bounding surfaces over a 250 mm × 100 mm footprint. Then, the pressure control points are placed on an XY plane onto which the plantar pressure maps are projected. Multiple candidate MM lattice types are compared, and the X lattice is selected based on the criteria. Finally, the X lattice infills the volume between two surfaces, with each rod's radius assigned using a distance- and pressure-weighted linear interpolation between 0.8 and 1.6 mm on nearby control points. These MM sole CAD geometries are used both to build the training set and as the under-OPT baseline for comparison with the DL-optimized designs.

Specifically, the 3D modeling of the shoe sole was conducted using software RHINOCEROS 3D 7 (from Robert McNeel & Associates TLM Inc., Seattle, WA). The initial outline of the sole was sketched by referring to the bottom and side views of the Adidas Ultraboost Light Core [56] shown in Step B of Fig. 1. In RHINOCEROS 3D 7, two 3D surfaces were created to match the side profile and top-bottom outline of the Adidas Ultraboost Light Core. These two surfaces are defined as the upper and lower boundaries, as shown in Fig. 5(*a*). In the top view, the length and width of the shoe sole are constrained within 250 mm × 00 mm, respectively, as these values are close to the median based on a survey study [57].

Within the 250 mm × 100 mm area, 25×10 pressure control points are generated to map the plantar pressure distribution. Between the two surfaces, $10 \times 4 \times 2$ central points are interpolated to position the MM lattice structure, with each lattice rod's

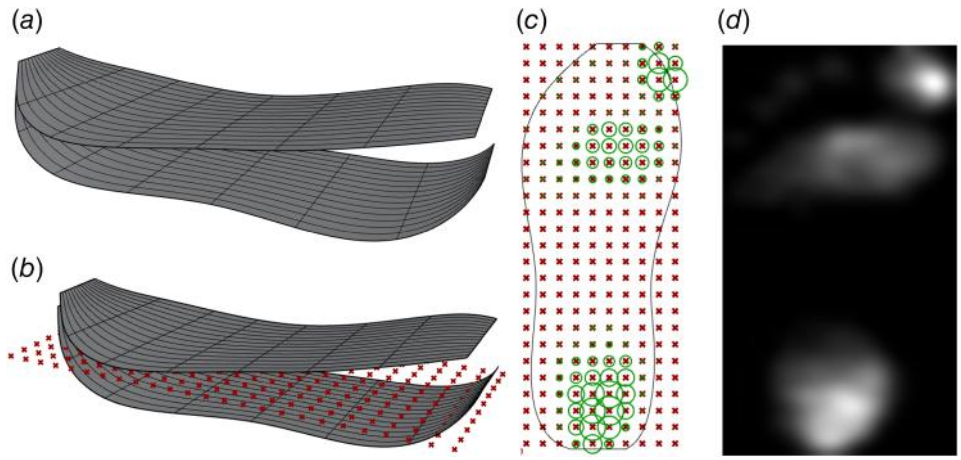

Fig. 5 The leveraged shoe sole outline and control points generation: (*a*) upper and lower surface, (*b*) plantar pressure and lattice structure control points, (c) map plantar pressure on control points, and (*d*) plantar pressure reference map

Table 1 Properties of the common lattice structures

Name	Mechanical properties
Cross	High strength, rigid, heavy duty
Diamond	Flexible, energy absorption, good cushioning
Grid	Uniform strength distribution, simple structure but lacks flexibility
Honeycomb	Lightweight, great cushioning, energy absorption, ideal for comfortable footwear
Octet	Isotropic in strength
Star	Stable, deformation resistant, heavy duty
Tesseract	Enhanced rigidity, heavy duty
Vintiles	Lightweight, flexible, good energy dissipation and impact absorption, good cushioning
X	Highly flexible, good impact resistance, isotropic

midpoint serving as the control point for the lattice structure. The two sets of control points are shown as red crosses in Fig. 5(*b*). The lattice structure control points in Fig. 5(*b*) are based on the *X* lattice structure, which will be discussed in Step C. The *X* lattice structure consists of 8 rods, resulting in 640 lattice structure control points displayed in the figure.

To visualize the approximate distribution of plantar pressure on the sole model, the high-resolution pressure map *S* is projected onto the 250 mm × 100 mm area, with each pressure control point's coordinates used to retrieve the corresponding pressure value from the image. In Fig. 5(*c*), the pressure magnitude is visualized as circles, with larger circles representing higher plantar pressure at the point. By comparing Figs. 5(*c*) and 5(*d*), it can be observed that the mapped pressure distribution is consistent with the reference pressure map.

3.3 Metamaterial Lattice Selection. Currently, several common types of lattice structures are used in MM and structural design [53], each with unique characteristics that fit specific applications. In Step C of Fig. 1, 10 different examples of lattice structures are listed, whose representative mechanical properties are summarized in Table 1 and used as the basis for selecting the *X* lattice in this study.

Given that this study is an initial attempt to optimize MM structures to improve sole deformation–pressure alignment, it is important to select a lattice structure that is uniform, isotropic, and easy to optimize. The *X* lattice structure is chosen for (1) it consists of only eight rods, which minimizes the number of components; (2) the rods are oriented in four directions, but each rod is vertical to the other three, making it one of the most isotropic structures; and (3) the *X* structure has no horizontal rods, eliminating the need for complex support structures and facilitating easier 3D printing. Figure 6(*a*) shows the result of filling the space between the surfaces with the *X* lattice structure. Each line segment represents a rod, while the dots are the lattice structure control points, which are the midpoints of each rod.

3.4 Metamaterial Sole Generation. In this study, the macroscopic mechanical properties of the lattice structure are modified by controlling the radius of each rod within the lattice. The radius of each rod in the MM structure is controlled by the distance to the nearest control point and the plantar pressure at that point. The plantar pressure values are scaled to the grayscale range from 1 to 255 by multiplying by a factor W_{reg}. This normalization ensures consistency across the dataset, allowing pressures of varying magnitudes to be compared and processed on the same scale.

For each control point, a preliminary radius value R_{base} is calculated by dividing the distance by the normalized pressure factor W_{reg}. This approach enables the model to account for pressure variations: areas with higher plantar pressure result in smaller base radii, while regions with lower pressure yield larger base radii. By correlating rod thickness to pressure, the structure can adapt to differing load requirements across the sole.

Finally, the R_{base} values are normalized within a practical range of 0.8–1.6 mm to determine the final rod radii. This step ensures that the radii remain within feasible structural integrity and manufacturability limits. Consequently, the rod radii are dynamically adjusted according to the plantar pressure distribution, allowing the MM structure to provide preliminary tailored support and cushioning.

The MM shoe sole structure generated based on this method is shown in Fig. 6(*b*). Extending the two upper and lower surfaces in Fig. 6(*a*) inward by 2 mm each, the sole's top and bottom solid surfaces are created to apply pressure and provide support. This results in an initial customized MM-based shoe sole CAD model driven by plantar pressure, as shown in Fig. 6(*c*). After obtaining the CAD model, the coordinates of each rod's midpoint and the radius of each rod are exported. These data will be used to train the DL model.

However, due to significant variations in the generated rod dimensions, 13 MM structures derived from plantar pressure data could not form effectively closed surfaces in RHINOCEROS 3D 7, preventing the generation of an FEA-ready CAD model. Consequently, the actual number of training samples used for the multimodal CNN model was 42.

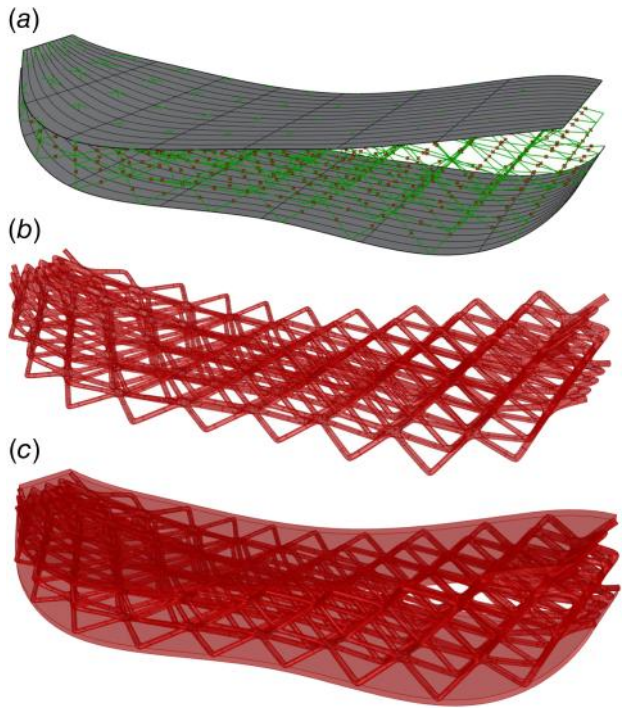

Fig. 6 MM-based shoe sole structure generation with *X* lattice: (*a*) shoe sole framework, (*b*) MM shoe sole structure with under-optimized radii, and (*c*) complete MM shoe sole CAD model

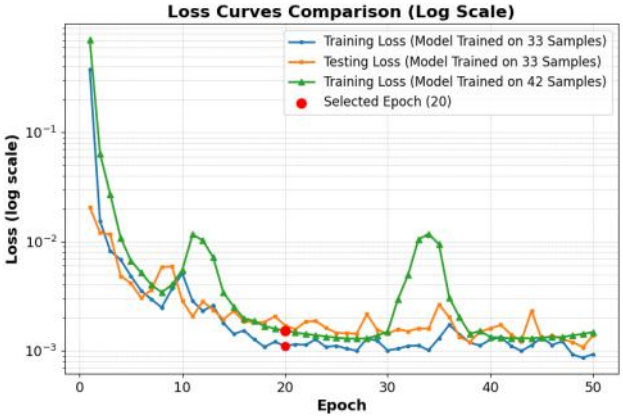

Fig. 7 Loss curves of the tailored multimodal CNN model

3.5 Finite Element Analysis–Deep Learning Model Setup. In this subsection, the coupling of the high-resolution FEA with a multimodal CNN is introduced in detail. In ANSYS, nine materials are simulated over under-optimized geometries under corresponding subject-specific pressure loads. The sole is meshed at about 0.4–0.47 million nodes, and nodewise *Z*-direction deformation is exported. The multimodal CNN model comprises three branches fusing pressure, geometry, and deformation to predict the MM rod radii.

3.5.1 Finite Element Analysis Setup. In ANSYS MECHANICAL 2024R2, nine kinds of materials are used for the MM structure generation. The key mechanical properties involved, including Young's modulus, Poisson's ratio, and density, are listed in Table 2.

Structural steel was used in our previous study [58]. The choice of structural steel for mechanical simulation is based on two primary considerations. First, in the elastic phase, structural steel exhibits a well-defined linear relationship between stress and strain. This simplifies the problem, enabling the DL model to more effectively map the relationship between pressure, actual/target deformation, and geometry. Additionally, many organic and inorganic materials also show linear or near-linear stress–strain behavior, so using a material with straightforward physical characteristics helps validate the feasibility and potential of this study's framework.

Second, from an application perspective, MM materials consist of numerous rods, inevitably leading to stress concentrations at the nodes, which require high fatigue resistance. Conventional 3D-printed organic materials have limited fatigue endurance, and with rod radii ranging only from 0.8 to 1.6 mm, elastic resins are generally insufficient to support body weight effectively. In practical applications, metal materials could be considered for the MM shoe sole structure, using tougher metals for the sole skeleton and foam as filler to achieve stress resistance, durability, and customizable pressure-adaptive deformation. Thus, simulating structural steel is a forward-looking approach.

With outstanding performance and potential, our inverse design framework shows with structural steel in our prior study [58], this study extended the materials employed to EVA, which is widely used in the shoe industry [59,60]. However, EVA is too soft when constructed as a lattice structure in MM shoe soles, given its Young's modulus ranging from 15 to 80 MPa [61]. With EVA as a constituent material for the MM shoe sole, the largest deformation can be as much as 50 mm, which is not realistic and acceptable for footwear.

Thus, we further extended the selection to materials with larger Young's modulus, including plastic ABS, polyethylene, epoxy resin, polyamide resin, polyester resin, and carbon fiber. The mechanical properties of the extended materials are given by ANSYS's engineering data sources [62]. It is worth noting that the carbon fiber material is anisotropic in Young's modulus. To assess whether anisotropy affects our model, two orthotropic carbon fiber cases with the principal fiber direction aligned with the global *X*- and *Y*-axes are evaluated, respectively, whose specific directional Young's moduli and Poisson's ratios are given in Table 2.

A tetrahedral FEA mesh is generated to discretize the MM solid structure of the shoe sole. The structure is meshed with sufficiently small elements to obtain high-resolution results (see Fig. 2(*b*)). The subsequent plantar pressures were applied to finer contact points on the upper surface. The total number of mesh nodes ranges from 386,885 to 466,870. Since the original image contains a total of 100,800 pixels, to simplify the FEA computation, pixels with grayscale values less than 1 are skipped in the image data. This method filters out approximately 30–60% of the area, which does not affect the FEA results because the pressure in these regions is too low to impact the structure. The skipped pressure nodes form a boundary for the plantar pressure imported into FEA. For a few un-skipped pressure nodes but outside the upper surface, they are not taken into consideration since the number of the nodes is small, and the pressure values are small. With the FEA model, deformation data of 466,870 nodes with their coordinates and *Z*-direction deformations will be exported as input for the DL model.

3.5.2 Deep Learning Model Setup and Training. The DL model is CNN-based, which captures features in the plantar pressure image and features in the structure and nodewise deformation. The DL model consists of three submodels to process three different inputs, as shown in Fig. 3.

The plantar pressure submodel processes normalized 2D pixel-wise grayscale plantar pressure images, with a resolution of 420×240. The submodel consists of three 2D convolutional layers with 3×3 kernels and filter sizes of 32, 64, and 128, respectively. Each convolutional layer is followed by ReLU activation and a max-pooling operation with a pooling factor of 2. The resulting feature maps are flattened and passed through a fully connected layer with 128 output units, capturing the spatial pressure characteristics for further processing.

The deformation submodel is designed to encode mechanical deformation data obtained from FEA simulations. Raw FEA outputs include the 3D coordinates and *Z*-direction deformation, enabling it to learn patterns in spatial deformation distribution. This submodel applies two 1D convolutional layers with kernel size 3 and filter sizes 64 and 128, respectively, each followed by

Table 2 Mechanical properties of the applied materials

Mechanical properties	Structural steel	Carbon fiber*X* (230 GPa)	Carbon fiber *Y* (230 GPa)	EVA	Plastic ABS	Polyethylene	Resin epoxy	Resin polyamide	Resin polyester
Young's modulus (GPa)	200	*X*: 230, *Y*: 23, Z: 23	*X*: 23, *Y*: 230, Z: 23	0.05	2.09	1.10	3.78	1.62	3.00
Poisson's ratio	0.3	*XY*: 0.2, *YZ*: 0.4, *XZ*: 0.2	*XY*: 0.2, *YZ*: 0.2, *XZ*: 0.4	0.32	0.4089	0.42	0.35	0.41	0.316
Density (kg/m^3)	7850	1800	1800	965	1030	950	1160	1140	1200

Table 3 Architecture of the proposed multimodal CNN models

Submodel	Input type	Input dimension	Layers	Kernel/pooling	Output dimension	Purpose
Pressure image network	Plantar pressure image	$420 \times 240 \times 1$	3×2D Conv + FC	Conv: 3×3 kernels, filters = 32/64/128 Max-pooling: factor 2 after each conv	128	Extract spatial features of plantar pressure distribution
Deformation network	FEA deformation data (nodewise)	$466{,}870 \times 4$	2×1D Conv	Conv: kernel size 3, filters = 64/128 Max-pooling: factor 2 after each conv	128	Encode high-resolution mechanical response patterns
Rod coordinates network	Rod midpoint coordinates	640×3	2×1D Conv	Conv: kernel size 3, filters = 32/64 Max-pooling: factor 2 after each conv	32	Preserve lattice geometry and spatial relationships
Feature fusion	Concatenated latent features	$128 + 128 + 32$	Concatenation	–	288	Fuse multimodal representations
Fully connected layer	Fused feature	288	FC + ReLU	FC neurons: 256	256	Learn joint nonlinear mapping
Output layer	Rod radii prediction	–	FC		640	Predict the radius of each lattice rod

ReLU activation and a max-pooling operation with a pooling factor of 2. The resulting feature maps are flattened into a single 128-dimensional latent representation, which serves as the deformation feature embedding and is subsequently fused with pressure and geometry features for rod-radius prediction.

The rod coordinates submodel processes the coordinates of the midpoints of the rods in the lattice structure, capturing spatial relationships among these control points. It includes two 1D convolutional layers with kernel size 3 and filter sizes 32 and 64, respectively, each followed by ReLU activation with a max-pooling operation with a pooling factor of 2. The resulting feature maps are flattened into a 32-dimensional latent representation, which is fused with pressure and deformation features for rod-radius prediction.

The outputs from these three submodels are concatenated along the feature dimension into a combined feature vector of size 288 ($128 + 128 + 32$). This combined vector is passed through a fully connected layer with 256 neurons, followed by a ReLU activation. A final fully connected output layer maps the fused features to a 640-dimensional vector, where each element corresponds to the predicted radius of an individual rod in the MM shoe sole structure. This end-to-end architecture enables simultaneous consideration of plantar pressure, mechanical response, and lattice geometry in a single forward pass.

These sub-models provide complementary representations of pressure, geometry, and deformation, enabling an integrated model to predict the optimized radii for rods in the MM shoe sole. This model receives three inputs, i.e., pressure image with resolution of 420×240, deformation data with shape of $N \times 4$, where N denotes the number of nodes, and rod coordinates with shape of 640×3. The number of nodes ranges from 386,885 to 466,870. This variation is due to differences in the 3D CAD models of the MM shoe sole, which lead to slightly different mesh generations.

To standardize input dimensions across samples without introducing cross-sample information, a copy-based data filling strategy is adopted. Specifically, for each sample, the node-wise deformation data matrix is expanded to a fixed target length equal to the maximum node count observed in the dataset (466,870 nodes). A matrix with 466,870 rows is first initialized, after which the original deformation data are copied sequentially into the expanded matrix to fill the remaining rows. This procedure does not introduce deformation information from other samples and preserves sample-level independence, while enabling uniform input sizing for the deformation submodel.

The multimodal CNN architecture used for model deployment is summarized in Table 3, which details the structure of each submodel, the associated input and output dimensions, and the feature fusion strategy. This table serves as a concise reference for the implemented network and facilitates reproducibility of the proposed inverse-design approach.

The combined model is trained on 42 samples for 50 epochs with a batch size of 4. Adam optimizer is applied with a learning rate of 0.001. The MSE loss is set as the criterion. At the preliminary exploration stage, the 42 available samples were split into a training set (33 samples) and a testing set (9 samples) using an 8:2 ratio. During training, both training loss and testing loss were recorded to assess convergence and overfitting behavior, as shown by the curves in Fig. 7. The loss evolution indicates that the model converges within the first 20 epochs, while occasional overfitting behavior (manifested as several peaks in testing loss) can be observed after approximately the 25th epoch.

Considering the severely limited sample size, training the model using all 42 samples was explored. The corresponding training loss, as shown in Fig. 7, exhibits a smoother trajectory compared with training on 33 samples, which generally indicates improved convergence stability. In addition, it is observed that loss (MSE) alone is not a fully reliable indicator of design quality in this inverse-design setting, as lower loss does not necessarily imply better regional alignment between deformation and plantar pressure distributions, particularly when the model is deployed using a prescribed target deformation as the third input.

Based on these considerations, all 42 samples were used for training in the final model deployment. As no testing loss was available to support an early stopping strategy, the model parameters at the end of the 20th epoch were selected for deployment, shown as the larger dots marked in Fig. 7, guided by the loss behaviors observed in both the split-training and all-sample training experiments. Accordingly, overfitting is mitigated by training on all available samples to improve convergence stability and by selecting the model at the 20th epoch, well before overfitting behavior is observed in preliminary experiments.

The multimodal CNN model thus effectively synthesizes features from diverse inputs, i.e., pressure, rod geometry, and deformation, enabling it to predict optimized rod radii tailored to the plantar pressure distribution and the structure's response to stress. This architecture captures complex interactions among the input variables and provides a comprehensive solution for optimizing the MM shoe sole structure.

3.6 Results and Discussion. In this subsection, the pipeline is validated via forward FEA by comparing DL-optimized designs to

under-optimized designs against target deformation. The DL designs consistently reduce MSE by roughly 48–80% relative to the under-OPT baseline. Minor differences in mesh size are observed under identical meshing settings. These results indicate that, compared with the under-OPT baseline, the DL-optimized designs exhibit deformation patterns that more closely match the prescribed target deformation, with increased deformation in high-pressure regions and reduced deformation in arch regions.

3.6.1 Forward Validation With Finite Element Analysis Simulation Results. This step is to use the trained multimodal CNN model and target deformation data to generate and validate the DL-optimized MM shoe sole geometry. Before generation, the target deformation should be defined according to the user's plantar pressure based on Eq. (2). Figure 8(*a*) shows the pressure weight distribution on the *XY* plane for FEA elements, and Fig. 8(*b*) illustrates the distribution of $T(x, y, z)$ after applying both w_p and w_z. Darker regions in Fig. 8(*b*) indicate areas where larger target deformations are intended.

Under this scenario, the plantar pressure of three individuals (C04, C24, C38) is used to generate MM shoe soles over nine materials. The newly generated MM shoe sole geometries are subjected again to the corresponding plantar pressure loading in the FEA simulation environment. This analysis yields *Z*-direction deformation results for the DL-optimized structures. Comparing these results with the target deformation, the MSE for the under-optimized structures and DL-optimized structures is obtained, as shown in Table 4. In this table, under-OPT models indicate the under-optimized models, while OPT models indicate the DL-optimized models.

From Table 4, the number of nodes for DL-optimized models is less than the number of nodes for under-optimized models for any individual with any material. The MSE of a model is calculated based on the mechanical response from FEA and the target deformation $T(x, y, z)$. The value of the MSE indicates whether the simulated mechanical response can comply with our expectations. A smaller MSE indicates closer agreement between the simulated deformation field and the prescribed target deformation $T(x, y, z)$, reflecting improved deformation–pressure alignment under the assumed surrogate formulation. As the Young's moduli for the materials are different, the observed deformation can vary by the order of magnitude. Thus, the MSE varies a lot by the order of magnitude as well. Materials with a larger Young's modulus have relatively lower MSE, while those with a smaller Young's modulus have relatively larger MSE. Yet, the comparison is between under-optimized models and DL-optimized models. Meanwhile, the percentage of MSE reduction can be used for between-group comparisons.

Given the percentage of MSE reduction in the last column, the DL-optimized MM shoe sole structures demonstrate substantial improvements in deformation tracking relative to the target deformation, with reductions ranging from 48% to 80% compared to under-optimized baselines, which suggests improved pressure-adaptive deformation behavior under the adopted surrogate formulation. It is worth noting that the smallest percentage of MSE reductions occurs when the material is structural steel, while the softest material, EVA, does not show further significant reduction. It might be caused by the structural steel's extremely high Young's modulus, but it needs to be further investigated.

Figure 9 shows an intuitive comparison of deformation between the under-optimized geometry and our proposed DL-optimized geometry. In this figure, it is noticeable that the DL-optimized geometry exhibits deformation patterns that more closely follow the plantar pressure distribution, particularly in high-pressure regions such as the big toe area. Meanwhile, the arch of the DL-optimized design is also much more solid according to the lower plantar pressure in Fig. 5(*d*).

3.6.2 Manufacturing Customized Metamaterial Shoe Sole. The prototype shoe sole was designed with optimized MM rod radii to demonstrate regionally varying mechanical characteristics under the proposed surrogate design objective. The design allows the sole to achieve nonuniform stiffnesses across multiple zones, resulting in a nonuniform stiffness distribution across different regions of the sole. Specifically, the forefoot and heel regions exhibit lower stiffness, while the arch regions exhibit relatively higher stiffness under the prescribed design parameters.

The DL-optimized MM shoe sole was brought into reality with additive manufacturing by a stereolithography machine, utilizing Elastic Resin to achieve the required flexibility and durability. This material was selected for its ability to support proof-of-concept fabrication rather than replicate the mechanical behavior of commercial footwear materials. The precise control offered by 3D printing enabled the accurate construction of the

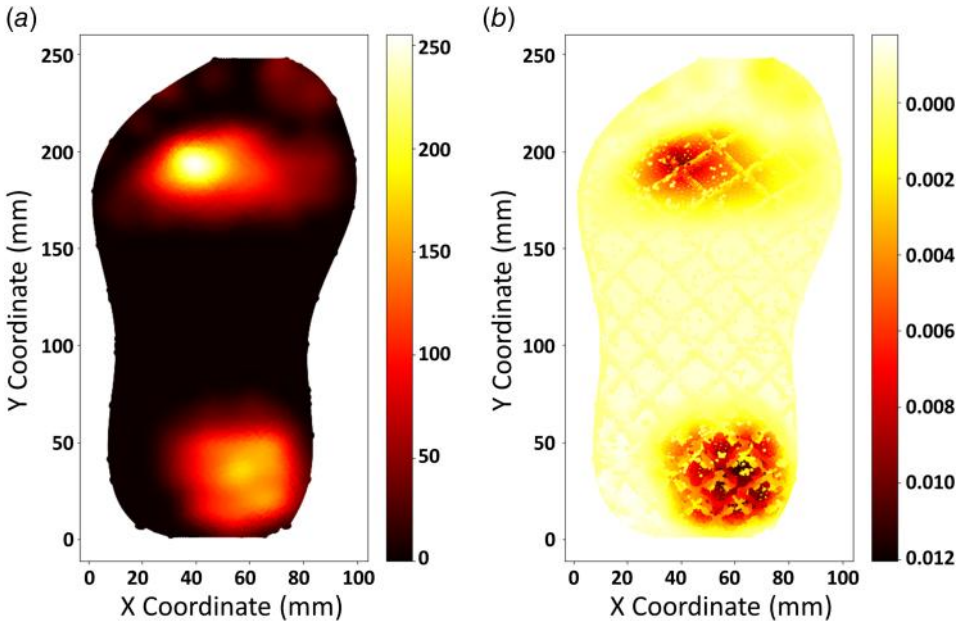

Fig. 8 (*a*) Heat map of the target deformation weighted by plantar pressure and (*b*) heat map of the target deformation weighted by both plantar pressure and *Z*-coordinates

Table 4 MSE comparison between under-optimized geometries and DL-optimized geometries

Part #	Material	# of nodes for under-OPT model	# of nodes for OPT model	MSE of under-OPT model (mm^2)	MSE of OPT model (mm^2)	% MSE reduction
C04	ST	465,244	459,987	6.75E−07	3.48E−07	48.55
C04	CF	465,244	460,624	7.05E−04	1.93E−04	72.59
C04	CFY	465,244	458,317	3.20E−04	1.06E−04	66.95
C04	EVA	465,244	460,158	1.63E+02	5.34E+01	67.26
C04	PABS	465,244	460,706	9.07E−02	3.37E−02	62.82
C04	PE	465,244	459,295	3.26E−01	7.25E−02	77.75
C04	REX	465,244	459,271	2.83E−02	7.64E−03	72.99
C04	RP	465,244	459,872	4.54E−02	1.55E−02	65.82
C04	RPA	465,244	457,250	1.51E−01	3.62E−02	76.03
C24	ST	464,471	460,053	7.55E−07	3.46E−07	54.19
C24	CF	464,471	460,110	9.04E−04	2.08E−04	77.00
C24	CFY	464,471	460,060	4.54E−04	1.18E−04	73.91
C24	EVA	464,471	458,417	2.02E+02	6.23E+01	69.13
C24	PABS	464,471	461,873	1.12E−01	4.67E−02	58.35
C24	PE	464,471	459,985	4.03E−01	7.91E−02	80.36
C24	REX	464,471	459,879	3.50E−02	7.84E−03	77.60
C24	RP	464,471	457,287	5.61E−02	1.05E−02	81.23
C24	RPA	464,471	458,884	1.87E−01	3.77E−02	79.79
C38	ST	464,740	458,270	4.45E−07	1.95E−07	56.25
C38	CF	464,740	457,238	1.32E−03	2.97E−04	77.61
C38	CFY	464,740	458,447	7.08E−04	1.83E−04	74.19
C38	EVA	464,740	460,408	2.98E+02	9.16E+01	69.28
C38	PABS	464,740	459,620	1.65E−01	3.97E−02	75.98
C38	PE	464,740	458,865	5.94E−01	1.44E−01	75.76
C38	REX	464,740	460,450	5.17E−02	1.67E−02	67.62
C38	RP	464,740	459,341	8.29E−02	2.32E−02	72.02
C38	RPA	464,740	460,329	2.22E−01	4.99E−02	77.50

intricate MM structure, faithfully reproducing the optimized rod radii and overall design. This step ensured that the DL-optimized design can be translated seamlessly into a functional physical prototype.

As shown in Step G of Fig. 1, the DL-optimized MM shoe sole prototype exhibits visually observable deformation behavior under applied loading. Specifically, Fig. 1(*a*) shows the sole's flexible structure, while Fig. 1(*b*) and 1(*c*) highlight how the sole compresses under applied pressure. These characteristics demonstrate the potential of MM-based soles to provide region-specific mechanical response through lattice-level geometric variation, highlighting the manufacturability of pressure-adaptive MM shoe sole designs under the proposed framework. This customized sole prototype shows the efficiency of MM design in footwear applications. The DL-optimized structure with adaptive support could serve as a foundation for future studies investigating pressure-adaptive mechanical responses using quantitative mechanical testing and human-subject evaluation.

3.6.3 Limitations and Outlook. In this study, linear-elastic materials are employed in FEA simulations to enable efficient structural design generation and model training for inverse design. While this assumption facilitates accelerated simulation and stable training, it does not capture the nonlinear behavior of real footwear materials, such as EVA foams and elastomeric polymers. Consequently, the simulated mechanical responses should be interpreted as relative deformation trends under a surrogate formulation rather than as a direct predictor of the real performance of footwear products.

The resin-based prototypes fabricated in this study serve as proof-of-concept realizations of the DL-optimized MM shoe sole structures and demonstrate the manufacturability of the proposed designs using additive manufacturing. For industrial footwear applications, this workflow can be extended by calibrating materials using experimental stress–strain data and incorporating nonlinear constitutive laws, such as hyperelastic or viscoelastic models, into the FEA–DL loop.

In addition, the present study adopts a static plantar pressure representation corresponding to a peak or maximum-pressure condition, rather than explicitly modeling time-resolved gait dynamics. This simplification is intentional and reflects the scope of this work, which aims to investigate the adaptation of MM shoe sole structures to static plantar pressure distributions within an inverse-design framework. The proposed methodology, case studies, and

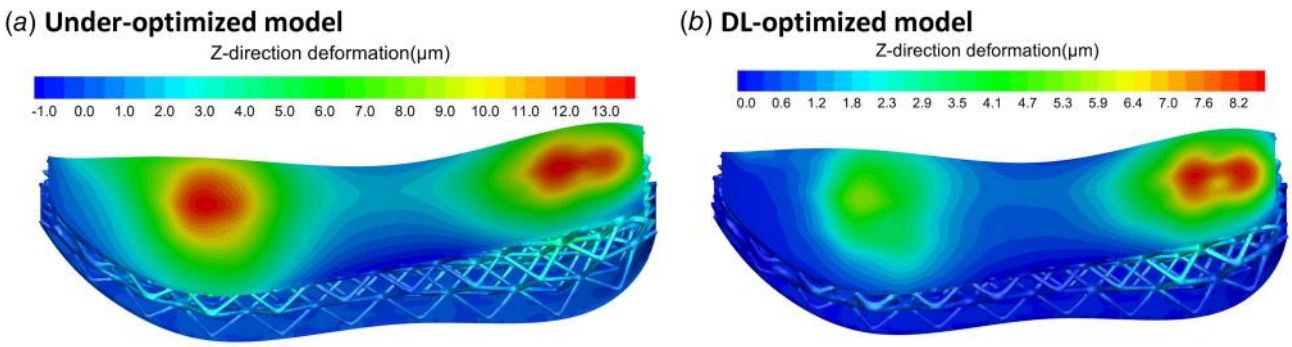

Fig. 9 FEA *Z*-direction deformation comparison: (*a*) under-optimized geometry and (*b*) DL-optimized geometry

resulting designs are therefore not intended to directly optimize or predict performance across different gait phases. While dynamic gait behavior is an important and unavoidable aspect of footwear biomechanics, incorporating multiphase or time-dependent loading would substantially increase modeling and data requirements. Extending the current framework to account for sequential gait phases or time-resolved pressure fields represents an important direction for future research.

While the present study focuses on *X*-lattice structures for relative isotropic mechanical behavior and reduced computational cost in training and optimization, the proposed framework is not restricted to a single lattice structure. Future work will be extended to include more lattice structures. To support topology-aware learning, graph-based representations and graph neural networks (GNNs) will be explored [63], enabling direct encoding of node connectivity and spatial relationships without reliance on fixed lattice layouts. Specifically, lattice structures can be represented as graphs by treating rod junctions as nodes and physical connections between junctions, which are rods, as edges. Node attributes may encode spatial coordinates, local mechanical responses, and design variables, while edge attributes can describe rod radii, rod length, rod angle, etc.

Finally, the proposed inverse-design framework inherently relies on the fidelity of the FEA model. Any modeling assumptions or simplifications in boundary conditions, contact modeling, or material behavior may propagate through the DL surrogate and influence the optimized designs.

4 Conclusions and Future Work

This study demonstrates the potential of MM-based shoe sole inverse design for customized footwear and develops a promising workflow that integrates FEA and DL for structural design and optimization. By leveraging DL to refine MM radii, the inversely designed shoe sole can achieve region-specific stiffness, better aligning with each user's unique plantar pressure distribution. With efficient and effective inverse design enabled by the proposed FEA–DL integration approach, the preliminary results also demonstrated significantly improved user-specific mechanical response and reductions in the deformation-tracking error ranging from 40% to 80% under the adopted surrogate formulation and FEA validation.

The target deformation proposed in this study is designed as a surrogate mechanical objective to guide inverse design and serve as an input for the DL model. Yet, this function can be further improved and more carefully designed. As this work has already demonstrated that the DL-optimized model can improve the deformation–pressure alignment to the target deformation, any designed target deformation can be used as the input for the trained DL model, and thus, the DL-optimized MM shoe sole structures can have a corresponding mechanical response. This flexibility highlights the potential of the framework for future customized or medical applications, although their specific effectiveness requires further investigation.

Future work will focus on extending the methodology framework to support more complex lattice structures and refining DL models, potentially through GNNs for spatial learning [64] and physics-informed deep learning [65]. Improvements in data acquisition strategies, such as data augmentation with machine learning models [66–68], will also be considered to support higher-fidelity training. On the simulation side, FEA will be expanded to investigate how different constituent materials influence the mechanical response of MM soles. Expanding FEA simulations to include more mechanical properties and dynamic performance analysis will further improve the model's practical utility. Additionally, performance metrics, including peak pressure reduction, fatigue life predictions, and other mechanically measurable indicators, will also be further explored to support the quantitative evaluation of the proposed framework. Furthermore, mechanical testing and human-subject studies will be considered to establish quantitative links between deformation–pressure alignment and perceived comfort, enabling more comprehensive experimental validation of the computational methodology.

Acknowledgment

The authors thank the Oklahoma State University CEAT Engineering Research & Seed Funding (ERSF) Program for the continued support.

Conflict of Interest

There are no conflicts of interest.

Data Availability Statement

The datasets generated and supporting the findings of this article are obtainable from the corresponding author upon reasonable request.

References

[1] Amorim, D. J. N., Nachtigall, T., and Alonso, M. B., 2019, "Exploring Mechanical Meta-Material Structures Through Personalised Shoe Sole Design," Proceedings of the Third Annual ACM Symposium on Computational Fabrication, Association for Computing Machinery, New York, NY, USA, pp. 1–8.

[2] Yang, W. Y., Zhuang, Y., Darcy, L. A., Liu, G., and Ion, A., 2022, "Reconfigurable Elastic Metamaterials," Proceedings of the 35th Annual ACM Symposium on User Interface Software and Technology, ACM, Bend, OR, USA, pp. 1–13.

[3] Hudak, Y. F., Li, J.-S., Cullum, S., Strzelecki, B. M., Richburg, C., Kaufman, G. E., Abrahamson, D., et al., 2022, "A Novel Workflow to Fabricate a Patient-Specific 3D Printed Accommodative Foot Orthosis With Personalized Latticed Metamaterial," Med. Eng. Phys., **104**(1), p. 103802.

[4] Feijs, L., Nachtigall, T., and Tomico, O., 2016, "Sole Maker: Towards Ultra-Personalised Shoe Design Using Voronoi Diagrams and 3D Printing," Proceedings of the Fabrication and Sculpting Event, pp. 31–40.

[5] Leung, M. S., Yick, K., Sun, Y., Chow, L., and Ng, S., 2022, "3D Printed Auxetic Heel Pads for Patients With Diabetic Mellitus," Comput. Biol. Med., **146**, p. 105582.

[6] Qiu, T., Shi, X., Wang, J., Li, Y., Qu, S., Cheng, Q., Cui, T., and Sui, S., 2019, "Deep Learning: A Rapid and Efficient Route to Automatic Metasurface Design," Adv. Sci., **6**(12), p. 1900128.

[7] Kazim, M., Pal, A., and Goswami, D., 2025, "Mechanical Metamaterials for Bioengineering: In Vitro, Wearable, and Implantable Applications," Adv. Eng. Mater., **27**(7), p. 2401806.

[8] Choukir, S., and Singh, C. V., 2023, "Role of Topology in Dictating the Fracture Toughness of Mechanical Metamaterials," Int. J. Mech. Sci., **241**, p. 107945.

[9] Pan, C., Han, Y., and Lu, J., 2020, "Design and Optimization of Lattice Structures: A Review," Appl. Sci., **10**(18), p. 6374.

[10] Yuan, S., Chua, C. K., and Zhou, K., 2019, "3D-Printed Mechanical Metamaterials With High Energy Absorption," Adv. Mater. Technol., **4**(3), p. 1800419.

[11] Bickel, B., Bächer, M., Otaduy, M. A., Richard Lee, H., Pfister, H., Gross, M., and Matusik, W., 2010, "Design and Fabrication of Materials with Desired Deformation Behavior," ACM Trans. Graph., **29**(4), pp. 1–10.

[12] Kuleyin, H., Budak, S., Yasan, ÖB, and Gümrük, R., 2025, "Characterization of Thermal, Chemical, Mechanical, and Fatigue Behavior of 3D Printed ABS-Based Elastomeric Blends: ABS/EVA and ABS/TPU," Polym. Test., **145**, p. 108763.

[13] Gao, S., Gain, A. K., and Zhang, L., 2021, "A Metamaterial for Wearable Piezoelectric Energy Harvester," Smart Mater. Struct., **30**(1), p. 015026.

[14] Duncan, O., Shepherd, T., Moroney, C., Foster, L., Venkatraman, P. D., Winwood, K., Allen, T., and Alderson, A., 2018, "Review of Auxetic Materials for Sports Applications: Expanding Options in Comfort and Protection," Appl. Sci., **8**(6), p. 941.

[15] Muir, B. C., Li, J.-S., Hudak, Y. F., Kaufman, G. E., Cullum, S., and Aubin, P. M., 2022, "Evaluation of Novel Plantar Pressure-Based 3-Dimensional Printed Accommodative Insoles—A Feasibility Study," Clin. Biomech., **98**, p. 105739.

[16] Maconachie, T., Leary, M., Lozanovski, B., Zhang, X., Qian, M., Faruque, O., and Brandt, M., 2019, "SLM Lattice Structures: Properties, Performance, Applications and Challenges," Mater. Des., **183**, p. 108137.

[17] Nickerson, K. A., Li, E. Y., Telfer, S., Ledoux, W. R., and Muir, B. C., 2024, "Exploring the Mechanical Properties of 3D-Printed Multilayer Lattice Structures for Use in Accommodative Insoles," J. Mech. Behav. Biomed. Mater., **150**, p. 106309.

[18] Cheng, H., Liu, B., Liu, M., and Cao, W., 2022, "Design of Three-Dimensional Voronoi Strut Midsoles Driven by Plantar Pressure Distribution," J. Comput. Des. Eng., **9**(4), pp. 1410–1429.
[19] Martínez, J., Hornus, S., Song, H., and Lefebvre, S., 2018, "Polyhedral Voronoi Diagrams for Additive Manufacturing," ACM Trans. Graphics, **37**(4), pp. 1–129:15.
[20] Kuwer Bugin, L. A., Machado Fagundes, C. V., Miotto Bruscato, U., and Alves Cândido, L. H., 2020, "Exploration of Data-Driven Midsole Algorithm Design Based in Biomechanics Data and Voronoi 3D to Digital Manufacturing," Des. Tecnol., **10**(21), pp. 1–10.
[21] Bauer, J., Meza, L. R., Schaedler, T. A., Schwaiger, R., Zheng, X., and Valdevit, L., 2017, "Nanolattices: An Emerging Class of Mechanical Metamaterials," Adv. Mater., **29**(40), p. 1701850.
[22] Cheng, X., Zhang, Y., Ren, X., Han, D., Jiang, W., Zhang, X. G., Luo, H. C., and Xie, Y. M., 2022, "Design and Mechanical Characteristics of Auxetic Metamaterial With Tunable Stiffness," Int. J. Mech. Sci., **223**, p. 107286.
[23] Ghavidelnia, N., Bodaghi, M., and Hedayati, R., 2021, "Idealized 3D Auxetic Mechanical Metamaterial: An Analytical, Numerical, and Experimental Study," Materials, **14**(4), p. 993.
[24] Hua, J., Lei, H., Gao, C.-F., Guo, X., and Fang, D., 2020, "Parameters Analysis and Optimization of a Typical Multistable Mechanical Metamaterial," Extreme Mech. Lett., **35**, p. 100640.
[25] Spahiu, T., Almeida, H., Ascenso, R. M. T., Vitorino, L., and Marto, A., 2021, "Optimization of Shoe Sole Design According to Individual Feet Pressure Maps," Comput. Ind., **125**, p. 103375.
[26] Mohammadi, M. M., and Nourani, A., 2025, "Machine Learning-Based Prediction of Compressive Energy Absorption in Shoe Soles With Different Features," Sci. Rep., **15**(1), p. 37059.
[27] Lu, Z., Li, X., Sun, D., Song, Y., Fekete, G., Kovács, A., András, K., and Gu, Y., 2025, "Parametric Cushioning Lattice Insole Based on Finite Element Method and Machine Learning: A Preliminary Computational Analysis," J. Biomech., **184**, p. 112674.
[28] Dong, G., Tessier, D., and Zhao, Y. F., 2019, "Design of Shoe Soles Using Lattice Structures Fabricated by Additive Manufacturing," Proc. Des. Soc. Int. Conf. Eng. Des., **1**(1), pp. 719–728.
[29] Menz, H. B., and Bonanno, D. R., 2021, "Footwear Comfort: A Systematic Search and Narrative Synthesis of the Literature," J. Foot Ankle Res., **14**(1), p. 63.
[30] Sidiqui, A. J., and Waris Khan, M. G., 2024, "Emerging Trends of Polymer Materials for Footwear Applications in India," Eng. Headway, **11**, pp. 17–26.
[31] Jenkins, M., 2003, *Materials in Sports Equipment*, Elsevier, New York.
[32] Che, H., Nigg, B. M., and de Koning, J., 1994, "Relationship Between Plantar Pressure Distribution Under the Foot and Insole Comfort," Clin. Biomech., **9**(6), pp. 335–341.
[33] Chatzistergos, P. E., Gatt, A., Formosa, C., Farrugia, K., and Chockalingam, N., 2020, "Optimised Cushioning in Diabetic Footwear Can Significantly Enhance Their Capacity to Reduce Plantar Pressure," Gait Posture, **79**, pp. 244–250.
[34] Melia, G., Siegkas, P., Levick, J., and Apps, C., 2021, "Insoles of Uniform Softer Material Reduced Plantar Pressure Compared to Dual-Material Insoles During Regular and Loaded Gait," Appl. Ergon., **91**, p. 103298.
[35] Salzano, M. Q., Weir, G., Thompson, J., Trudeau, M. B., Ertel, C., Dear, K., Willwacher, S., and Hamill, J., 2022, "Can Footwear Satisfaction Be Predicted From Mechanical Properties?," Footwear Sci., **14**(3), pp. 151–161.
[36] Lane, T. J., Landorf, K. B., Bonanno, D. R., Raspovic, A., and Menz, H. B., 2014, "Effects of Shoe Sole Hardness on Plantar Pressure and Comfort in Older People With Forefoot Pain," Gait Posture, **39**(1), pp. 247–251.
[37] Goonetilleke, R. S., and Luximon, A., 2001, "Designing for Comfort: A Footwear Application," Proceedings of the Computer-Aided Ergonomics and Safety Conference, Maui, HI.
[38] Abu-Mualla, M., and Huang, J., 2023, "Inverse Design of 3D Cellular Materials With Physics-Guided Machine Learning," Mater. Des., **232**, p. 112103.
[39] Zolfagharian, A., Lakhi, M., Ranjbar, S., and Bodaghi, M., 2021, "Custom Shoe Sole Design and Modeling Toward 3D Printing," Int. J. Bioprint., **7**(4), p. 396.
[40] Tang, Y., Dong, G., Xiong, Y., and Wang, Q., 2021, "Data-Driven Design of Customized Porous Lattice Sole Fabricated by Additive Manufacturing," Procedia Manuf., **53**, pp. 318–326.
[41] Kumar Singh, S., Rai, R., Pradip Khawale, R., Patel, D., Bielecki, D., Nguyen, R., Wang, J., and Zhang, Z., 2024, "Deep Learning in Computational Design Synthesis: A Comprehensive Review," ASME J. Comput. Inf. Sci. Eng., **24**(4), p. 040801.
[42] Xie, J., Zhang, C., Sun, L., and Zhao, Y. F., 2024, "Fairness- and Uncertainty-Aware Data Generation for Data-Driven Design Based on Active Learning," ASME J. Comput. Inf. Sci. Eng., **24**(5), p. 051004.
[43] Ha, C. S., Yao, D., Xu, Z., Liu, C., Liu, H., Elkins, D., Kile, M., et al., 2023, "Rapid Inverse Design of Metamaterials Based on Prescribed Mechanical Behavior Through Machine Learning," Nat. Commun., **14**(1), p. 5765.
[44] Zheng, X., Zhang, X., Chen, T.-T., and Watanabe, I., 2023, "Deep Learning in Mechanical Metamaterials: From Prediction and Generation to Inverse Design," Adv. Mater., **35**(45), p. 2302530.
[45] Zhilyaev, I., Krushinsky, D., Ranjbar, M., and Krushynska, A. O., 2022, "Hybrid Machine-Learning and Finite-Element Design for Flexible Metamaterial Wings," Mater. Des., **218**, p. 110709.
[46] Oladipo, B., Matos, H., Krishnan, N. M. A., and Das, S., 2023, "Integrating Experiments, Finite Element Analysis, and Interpretable Machine Learning to Evaluate the Auxetic Response of 3D Printed Re-Entrant Metamaterials," J. Mater. Res. Technol., **25**, pp. 1612–1625.
[47] Lubowiecka, I., Armesto, J., Arias, P., and Lorenzo, H., 2009, "Historic Bridge Modelling Using Laser Scanning, Ground Penetrating Radar and Finite Element Methods in the Context of Structural Dynamics," Eng. Struct., **31**(11), pp. 2667–2676.
[48] Logan, D. L., 2011, *A First Course in the Finite Element Method*, 5th ed., CL Engineering, Stamford, CT.
[49] Sun, Y., Zhou, Q., Niu, W., Zhang, S., Yick, K.-L., Gu, B., and Xu, W., 2024, "3D Printed Sports Shoe Midsoles: Enhancing Comfort and Performance Through Finite Element Analysis of Negative Poisson's Ratio Structures," Mater. Des., **245**, p. 113292.
[50] Song, Y., Shao, E., Bíró, I., Baker, J. S., and Gu, Y., 2022, "Finite Element Modelling for Footwear Design and Evaluation: A Systematic Scoping Review," Heliyon, **8**(10), p. e10940.
[51] Teixeira, R., Coelho, C., Oliveira, J., Gomes, J., Pinto, V. V., Ferreira, M. J., Nóbrega, J. M., da Silva, A. F., and Carneiro, O. S., 2021, "Towards Customized Footwear With Improved Comfort," Materials, **14**(7), p. 1738.
[52] Ulerich, O., Cananau, S., Prisecaru, D. A., Mărgăritescu, M., and Negrea, C.-S., 2024, "Design of Customized Shoe Soles Using Lattice Structures Fabricated by Additive Manufacturing," *Intelligent Systems in Production Engineering and Maintenance III*, A. Burduk, A. D. L. Batako, J. Machado, R. Wyczółkowski, E. Dostatni, and I. Rojek, eds, Springer Nature Switzerland, Cham, pp. 209–228.
[53] Kurtz, A., Tang, Y., and Zhao, F., 2015, "Intralattice, Generative Lattice Design With Grasshopper," https://github. com/dnkrtz/intralattice
[54] Patil, S. L., Thatte, M. A., and Chaskar, U. M., 2009, "Development of Planter Foot Pressure Distribution System Using Flexi Force Sensors," Sens. Transducers, **108**(9), pp. 73–79.
[55] Booth, B. G., Keijsers, N. L. W., Huysmans, T., and Sijbers, J., 2018, "The CAD WALK Healthy Controls Dataset". .
[56] "Ultraboost Shoes," Adidas US. https://www.adidas.com/us/ultraboost, Accessed April 16, 2026.
[57] Jurca, A., Žabkar, J., and Džeroski, S., 2019, "Analysis of 1.2 Million Foot Scans From North America, Europe and Asia," Sci. Rep., **9**(1), p. 19155.
[58] Zhang, Z., Feng, Y., and Liu, C., 2025, "Machine Learning and Finite Element Analysis Teaming for Inverse Design of Metamaterial With Adaptive Pressure Response in Footwear Design," 45th Computers and Information in Engineering Conference (CIE), Anaheim, CA, Aug. 17–20.
[59] Wang, L., Hong, Y., and Li, J. X., 2012, "Durability of Running Shoes With Ethylene Vinyl Acetate or Polyurethane Midsoles," J. Sports Sci., **30**(16), pp. 1787–1792.
[60] Swathy, K. K., Verma, R., and Kumar, L., 2023, "Ethylene-Vinyl Acetate Foam," *Polymeric Foams: Fundamentals and Types of Foams (Volume 1)*, R. K. Gupta, ed., American Chemical Society, Washington, DC, pp. 205–221.
[61] Dias, R. B. e., Coto, N. P., Batalha, G. F., and Driemeier, L., 2018, "Systematic Study of Ethylene-Vinyl Acetate (EVA) in the Manufacturing of Protector Devices for the Orofacial System," *Biomaterials in Regenerative Medicine*, L. A. Dobrzański, ed., IntechOpen, London, UK, pp. 319–340.
[62] Stolarski, T., Nakasone, Y., and Yoshimoto, S., 2018, *Engineering Analysis with ANSYS Software*, 2nd ed., Butterworth-Heinemann, Oxford, UK.
[63] Bian, S., Grandi, D., Liu, T., Jayaraman, P. K., Willis, K., Sadler, E., Borijin, B., et al., 2023, "HG-CAD: Hierarchical Graph Learning for Material Prediction and Recommendation in Computer-Aided Design," ASME J. Comput. Inf. Sci. Eng., **24**(1), p. 011007.
[64] Naghavi Khanghah, K., Wang, Z., and Xu, H., 2024, "Reconstruction and Generation of Porous Metamaterial Units via Variational Graph Autoencoder and Large Language Model," ASME J. Comput. Inf. Sci. Eng., **25**(2), p. 021003.
[65] Pan, L., Li, G., Zhu, T., Liu, D., Wang, Y., and Lu, Y., 2025, "Physics-Informed Machine Learning in Design and Manufacturing: Status and Challenges," ASME J. Comput. Inf. Sci. Eng., **25**(12), p. 120804.
[66] Kim, Y., Kim, Y., Yang, C., Park, K., Gu, G. X., and Ryu, S., 2021, "Deep Learning Framework for Material Design Space Exploration Using Active Transfer Learning and Data Augmentation," NPJ Comput. Mater., **7**(1), p. 140.
[67] Yangue, E., Fullington, D., Smith, O., Tian, W., and Liu, C., 2024, "Diffusion Generative Model-Based Learning for Smart Layer-Wise Monitoring of Additive Manufacturing," ASME J. Comput. Inf. Sci. Eng., **24**(6), p. 060903.
[68] Jeong, I., Kim, H., Cho, H., Park, H., and Kim, T., 2023, "Initial Structural Damage Detection Approach via FE-Based Data Augmentation and Class Activation Map," Struct. Health. Monit., **22**(5), pp. 3225–3249.